Chapter 3

Synthesis and Electrochemical Performances of Fluffy Carbonized Hexagonal $KCoPO_4$ as Pseudocapacitive Electrode for High performing Hybrid Supercapacitor Applications

3.1 Introduction

Fossil fuel energy, such as coal, natural gas, and liquid fuels, constitute the most important power source for electricity generation. The dependence on fossil fuels poses two important challenges: their inevitable exhaustion as finite sources and the severe negative environmental effects through their emissions of greenhouse gases. Worrying about such factors is, therefore, an essential matter when considered globally, since demand for such sustainable, clean solutions will continue to rise. Among the promising approaches for alleviating these challenges is the development and implementation of electrochemical energy storage systems. These systems can effectively store alternative energy, including power from renewable sources like solar panels and wind turbines, for continuous use.[1]-[4] A variety of energy storage technologies, such as batteries and electrochemical energy storage devices (EESDs), have emerged over the years as potential solutions.[1] Of these, Supercapacitors (SCs) and aqueous rechargeable batteries have received much attention as potential large-scale energy storage strategies. [5–9]

Supercapacitors, with their excellent power density, fast charge-discharge capability, and good cyclability, have been identified as suitable candidates for applications where short bursts of high energy are required. However, the energy density of a Supercapacitor is relatively low as compared to traditional batteries and, therefore, Supercapacitor do not represent as an option for long-term energy storage applications. Hence, aqueous rechargeable batteries have advantages in safety, cost-effectiveness, and environmental compatibility. These batteries are inherently safer and more sustainable because they use water-based electrolytes, compared to non-aqueous systems.[6] However, they have major drawbacks, such as poor cyclability and relatively low power density, which limit their application in electricity-demanding applications.[10]

Supercapacitors have emerged as a promising energy storage technology, especially for high-power applications, based on their excellent power density and the ability to charge and discharge rapidly. The available conventional batteries store electrochemical energy through chemical reactions, whereas Supercapacitors store electrochemical energy electrostatically, the batteries are more responsive and efficient to deliver power. However, traditional Supercapacitors suffer from some limitations in energy density, which restricts their adoption for applications in energy storage.

To address this issue, Hybrid or Asymmetric Supercapacitors have been developed. Advanced devices that combine the features of two different types of electrodes—typically a battery-type faradic electrode (which stores energy via redox reactions) and a capacitor-type electrode (which stores energy electrostatically)—can be used. This combination allows Hybrid Supercapacitors to achieve significantly higher energy density while maintaining a considerable power density, improved rate capability, and longer operational lifespan. Such properties make Hybrid/ Asymmetric Supercapacitors very attractive candidates for next-generation electrochemical energy storage devices (EESDs).[11]

One of the significant breakthroughs in Supercapacitor technology is the replacement of flammable and toxic organic electrolytes with aqueous electrolytes. Aqueous electrolytes enhance the electrochemical performance of Supercapacitors as well as it ensures greater safety and improve environmental concern. Regarding this, an aqueous Asymmetric Supercapacitor (AASc) shows a higher specific capacitance than a conventional electrical double-layer capacitor (EDLCs). This results from the effective charge storage mechanism facilitated by the aqueous electrolyte and the synergy between faradic and capacitive processes in the Asymmetric configuration.

In addition, AASc devices exhibit a characteristic diagonal Ragone plot, which is an energy density versus power density graphical representation. [11-15] This diagonal behavior shows AASc's ability to deliver both power and energy densities simultaneously, which is never possible with conventional energy storage devices. Such a trend in performance makes AASc highly suitable for applications where simultaneous quick power delivery and extended energy output are required-for example, electric vehicles, portable electronics, and grid-scale energy systems.

Despite these advantages, Supercapacitors, such as AASc, still face some challenges that limit their wider application. The first limitation is that the cycle stability of the Supercapacitor is poor at longer usage, which in turn limits its long-term durability. Supercapacitors also suffer from low specific energy, often restricting the storage of significant amounts of energy for a longer period. Furthermore, the fast-charging rate at constant electrochemical performance continues to be a challenge. [11-13]

A much-required need is for innovative material designs and new architectures of the devices. Novel electrode material designs should show improved electrical conductivity, with large surface area and great electrochemical stability; in that respect, the performances of the aqueous Asymmetric Supercapacitors can greatly be improved. For example, one might include nanostructured materials, metal oxides, carbon-based composites, or advanced Hybrid materials; then, their ability to carry high energy densities, deliver a better charge-discharge efficiency, and increase longer life cycles becomes evident. It is really critical for the realization of next-generation Supercapacitors that can suffice the increase in modern technologies.

The electrode materials for Supercapacitor applications have been widely explored by researchers. They involve transition metal oxides [16-17], sulfates [18-19], oxalates [20-22], and phosphates [23-25]. Polyanionic framework materials include a wide range of anion groups, denoted as $XO_4)^{n-}$ tetrahedra (where X = P, S, As, Si) covalently bonded with M-O polyhedra

(where M = Fe, Ni, Mn, Co, Ti, V, Cr). The open pore structure of these materials enhances ion transport during charge-discharge cycles and allows the active participation of the $M^{n/n+1}$ redox couple. The strong X-O bond in the tetrahedral structure increases ionicity in the M-O bond, reducing its covalent character and making the material suitable for high-voltage operation [23-26]. In addition, the X-O bond is added to provide the oxygen stability of the lattice, hence making the electrode material polyanionic type safe for high-rate charge storage and delivery. Consequently, polyanion materials are favorable over the rest of the transition metal-based compounds due to their structure's thermally stability and little volume expansion during charging and discharging. Specifically, promising positive electrode candidates in energy storage devices include cobalt-based phosphates like γ-KCoPO4 [25], $NaMn_{1/3}Ni_{1/3}Co_{1/3}PO_4$ [29], $KCo_xNi_{1-x}PO_4.2H_2O$ [30], $Co_3(PO_4)_2 \cdot 8H_2O$ [31], $Co_2P_2O_7$/MWCNT [32], and $Co_3(PO_4)_2$ [33], with outstanding redox activity, 3D ion transport channels, earth abundance, affordability, sustainability, and environmental friendliness.

This work details the sol-gel preparation of fluffy carbonized hexagonal $KCoPO_4$, which, by calcination, serves as a positive electrode material displaying high capacitance and long cycle life in aqueous Asymmetric Supercapacitors. The specific capacitance of the carbonized $KCoPO_4$ was determined as 725 F/g under a current density of 0.5 A/g, accompanied by good cyclic stability. Aqueous Asymmetric Supercapacitor containing $KCoPO_4$ as positive electrode and activated carbon as negative electrode was prepared as $KCoPO_4$//AC, tested in the 2M KOH aqueous electrolyte. In this device, an excellent energy density of 121.1 Wh/kg and a remarkable power density of 6945 W/kg with a working potential window of 1.5V were observed in the 2M KOH electrolyte.

3.2 Material synthesis and characterization

3.2.1 Synthesis of Fluffy Carbonized Hexagonal $KCoPO_4$

The Fluffy carbonized hexagonal $KCoPO_4$ was prepared by sol-gel process and followed by calcination of precipitate by raising the temperature to get the crystalline material. Precursors of analytical grade were utilized in deionized water (DI) (resistivity = 18.0 MΩ, pH = 7) for entire solution preparation and for whole study. 1mM Cobalt(II) Nitrate Hexahydrate ($Co(NO_3)_2 \cdot 6H_2O$, Merck 99.0%), 1mM of Potassium Nitrate (KNO_3, Merck 99.0%), and 1 mM of Ammonium phosphate ($NH_4H_2PO_4$, Merck 99.0%), and 3mM of Maleic Acid ($HO_2CCH=CHCO_2H$, Merck, 99%) was taken for synthesis of materials. Maleic acid was utilized as a chelating agent in near neutral pH solution containing K^+, $Co^{+,}$ and PO_4^{3+} ions it easily contributed to the production of carbonized powder after synthesis.

Firstly, the solution of 1mM of $Co(NO_3)_2.6H_2O$ and 1mM KNO_3 was prepared in 200 ml DI water at 80°C, this solution exhibit light pale red color. Subsequently, 1mM of $NH_4H_2PO_4$ was added to the solution that is mentioned above and followed by the addition of 3mM Maleic acid at the same temperature of 80°C. After mixing of all the precursors temperature of the gel mixer raised to 200°C for dry out the material. After drying the material extracted the material from beaker and ground it by using the agate mortar pestle and kept in muffle furnace at 600°C for 8 hours. Combustion of organic ligands due to the presence of C=C moiety at elevated temperature followed by evolution of CO_2 take place, the indigo blue-colored carbonized fluffy powder was obtained after grinding of calcined material.

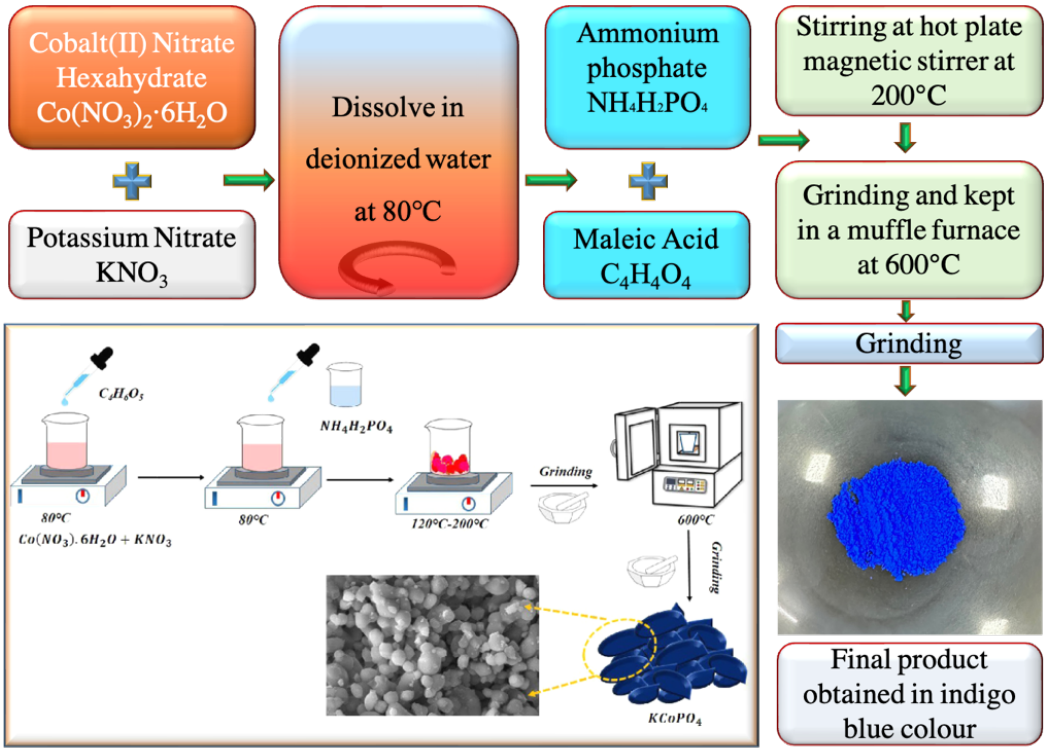

Figure 3.1: Synthesis route for the $KCoPO_4$ material preparation

3.2.2 Materials characterization

The crystal structure and purity of the compound were investigated by using a benchtop powder X-ray diffractometer (Rigaku miniflex 600) with Cu Kα radiation (λ = 1.54056 Å) in the 10-60° 2^i range and a step size of 0.02, The structure was matched using X'Pert High Score Plus (PANalytical); the materials' subsequent crystal structure was established using FullProf Suite software and the Rietveld refinement process. The material morphological analysis was conducted utilizing an EVO - Scanning Electron Microscope (SEM) MA15 / 18 CARL ZEISS and FTIR spectra were recorded in range of 400-4000 cm^{-1} wavenumber by using FTIR spectrometer (Nicolet 6700, Thermo Scientific). Pore size distribution and specific surface area of the sample were measured by BET (MicrotracBEL), With the aid of N2 adsorption/desorption isotherms at 77 K. For the analysis of carbon content in intermediate sample a thermogravimetric analysis (TGA) test was performed by using a Shimadzu TGA-50 analyzer.

3.2.3 Electrochemical Studies

All electrochemical performances of the sample including cyclic voltammetry (CV), galvanostatic charge-discharge (GCD), and electrochemical impedance spectroscopy (EIS) measurements were conducted in a conventional three-electrode arrangement and measured by Metrohm Autolab (PGSTAT204) equipped with FRA32 M module. Electrochemical measurements were analyzed using NOVA1.1 software.

3.2.4 Electrode Preparation

For a three-electrode arrangement, Hg/HgO (1M KOH) was used as the reference electrode, and platinum plate as the counter electrode. $KCoPO_4$ working electrodes were prepared by taking active material, activated carbon (AC), and binder polyvinylidene difluoride (PVDF) in the ratio of 70: 20: 10 weight % in N-methyl-2-pyrrolidone (NMP) solvent. The homogenous slurry was prepared with the help of agate mortar pestle and the slurry was cast over Toray carbon paper (Alfa Aesar). The materials (paste) loading was 1.4 mg over 1 cm^2 area of the coated electrode was dried at 80 ºC for 12 hrs. in oven. The total weight of material on the electrode was calculated by the difference between the weight of the material loaded electrode and the weight of the blank electrode by using Shimadzu electronic weighing balance machine of error limit: 0.01 mg. Consequently, the dried electrode was investigated for the three-electrode electrochemical analysis of the material. For the full cell two-electrode test (Asymmetric Supercapacitor), electrochemical study fluffy carbonized $KCoPO_4$ was use as the positive electrode and Activated carbon as the negative electrode in 2M KOH electrolyte.

3.3 Result and discussion

3.3.1 X-ray diffraction (XRD) analysis

The powder XRD pattern of prepared $KCoPO_4$ (calcined at 600°C for 8 h) sample was analyzed in the 2θ range of 10–60º with step size 0.02º by powder XRD study. Phase identification was done by Philips X'Pert High Score Plus and the XRD peak profile matches with the reference peak (JCPDS No.: 82-0762) of hexagonal $KCoPO_4$. All the aforementioned diffraction peaks with their respective positions and intensities correspond to the hexagonal phase with the space group $P6_3$ (S.G. No.: 173) with obtained refinement parameters R_p= 8.7, R_{wp}= 7.3, R_{exp} = 8.54, χ^2= 2.75, Rietveld refinement of the XRD profile of fluffy carbonized $KCoPO_4$ shown in the **figure 3.2(a)** and the **figure 3.2(b)** shows the VESTA image that confirms the 3D framework in which the presence of Phosphate (PO_4^{3-}) tetrahedral is connected by the corner of Co-O bonds and the presence of Co^{2+} ions in a tetrahedral environment.

3.3.2 FTIR Analysis

FT-IR spectrums of $KCoPO_4$ powder samples are shown in **figure 3.2(c)** revealing the presence of different functional groups at different wavenumber in range of 400-4000 cm^{-1}. The broad peak at 3400 cm^{-1} is ascribed to the stretching vibration of a hydroxyl group (–OH) which signifies the presence of water in the compound. Peak at 1635 cm^{-1} and 1386 cm^{-1} attributed to low bending mode water molecule.[34] A strong band arose at 1112 cm^{-1} and 1038 cm-1 due to asymmetric stretching(ν_{as}) of P-O bond vibration (990-1200cm^{-1}).[34] Peaks at 620 cm^{-1} referred to O-P-O out-plane bending and 428 cm^{-1} referred to -δPO_4 group. The Asymmetric stretching modes of CoO_6 tetrahedra have been observed at 585 cm-^{1} and the peak observed around 549 cm^{-1} may be ascribed to the Asymmetric stretching of Co–O bonds in CoO_6 octahedra.[35],[36] Additionally, the absorption peak at 479 cm^{-1} also arises due to the in-plane bending vibration of the O-P-O bond of the -PO_4 group. Thus, the major vibrational spectra validate the presence of the -PO_4 group in $KCoPO_4$.

3.3.3 Brunauer-Emmett-Teller (BET) Analysis

To further discuss the surface area and pore volume of the sample, the isotherm of N_2 adsorption-desorption at 77 K shown in BET image, given in the **figure 3.2(d)**. The isotherm corresponds to a type III isotherm that possesses a hysteresis loop of the H3 type.[37],[38] Previous studies indicate that the type III isotherms are usually found in non-rigid particle aggregates, or when the pore network contains macropores that are not filled by pore condensate. Because of this, the adsorption and desorption branches overlap at a higher P/Po value. [39],[40] This clearly points towards the existence of mesoporous structures that are interconnected with macropores with a specific surface area of the sample equivalent to 16.2 m^2/g, with the major pore size distribution varying between 3 and 10 nm, along with a few macro pores (~210 nm), as deduced from the BJH (Brunauer, Joyner, and Halenda) plot (inset in the **figure 3.2(d)**). The mesopores of the material resulted in improved electrochemical performance of the material because of high porosity of the material. The calculated average pore diameter of the $KCoPO_4$ sample was about ~46.39 nm. These pores of the material can facilitate the diffusion of electrolyte ion, including OH^- ion, and the redox reactions by greatly increasing the surface area of the active electrode.[41]

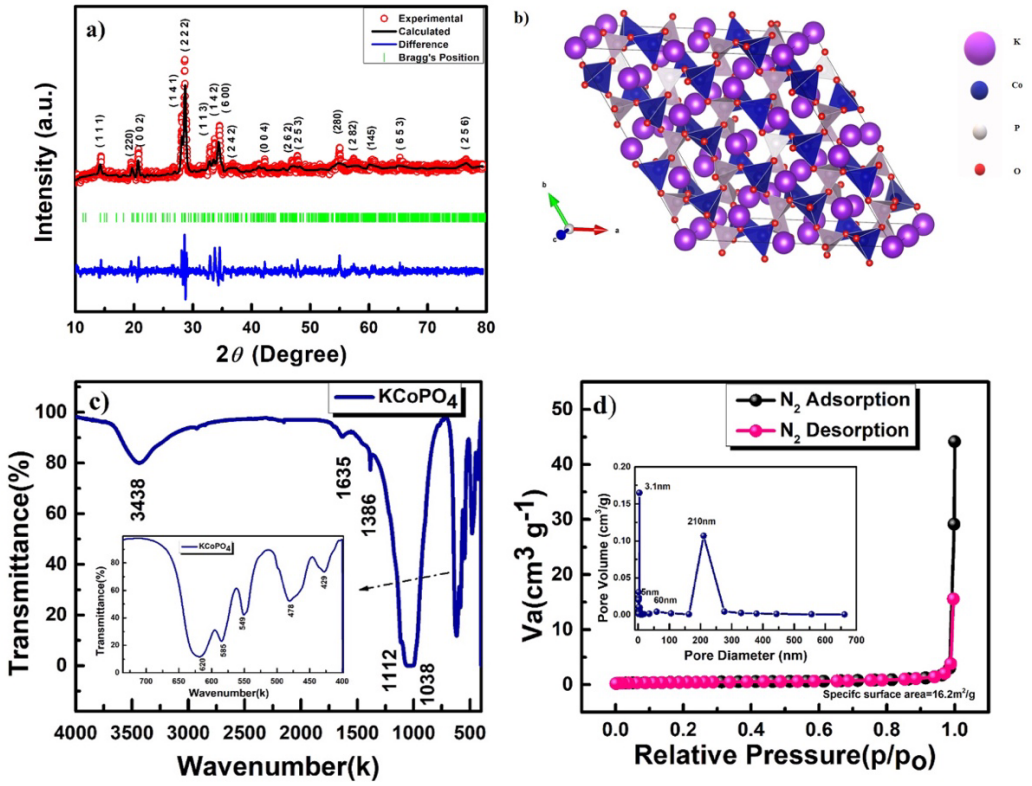

Figure 3.2: (a) XRD Rietveld refinement pattern of the $KCoPO_4$ powder sample, (b)VESTA image of $KCoPO_4$ (c) FTIR spectrum of $KCoPO_4$, and (d) N_2 adsorption/desorption isotherm of the $KCoPO_4$ sample

3.3.4 TGA Analysis

The **figure 3.3** shows a Thermogravimetric (TGA) analysis of an intermediate complex prepared $KCoPO_4$ at 200°C was finally annealed at 600°C were confirmed by Thermogravimetric (TGA) behavior measured in flowing air at 10°C/min ramping rate. Initial weight loss of approximately 2.05% has been observed due to presence of water and volatile substance present in the intermediate sample. Further, carbon loss of 5.55% was confirmed from 400°C to 600°C.

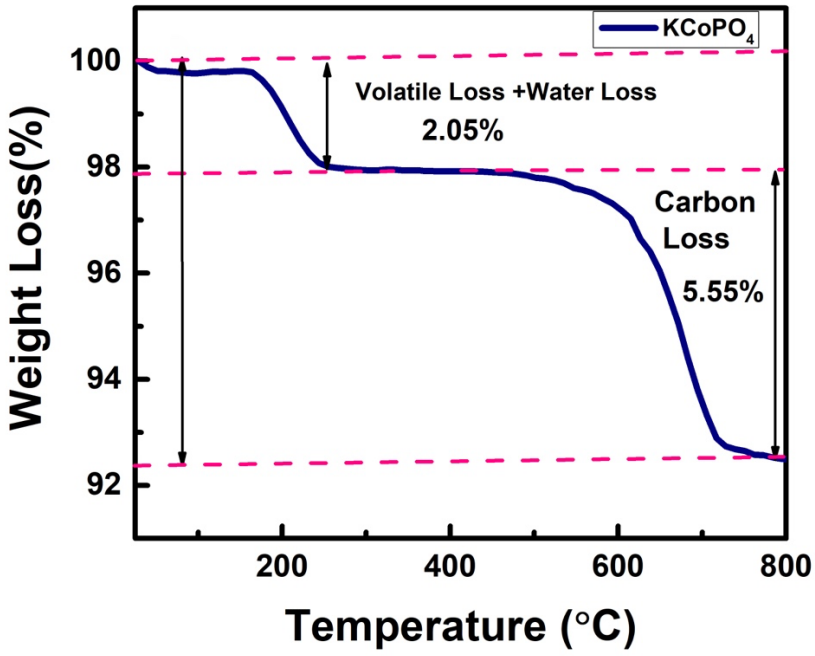

Figure 3.3: Thermogravimetric analysis (TGA) of $KCoPO_4$

3.3.5 X-ray photoelectron spectroscopy (XPS) Analysis

By XPS technique, the chemical composition along with the valence states were determined for the sample of $KCoPO_4$.

The wide-range survey spectrum presented in **figure 3.4(a)** confirms the presence of all the elements, that are, K, Co, P, and O. As shown in **figure 3.4(b)**, the binding energy values of K $2p_{3/2}$ at 292.5 eV and K $2p_{1/2}$ states at 295.2 eV indicate the existence of K^+ ions in the sample. **Figure 3.4(c)** shows the Co(2p) spectrum, which contains peaks due to the $2p_{3/2}$ state of Co^{2+} at 781.3 eV and the $2p_{1/2}$ state at 797.31 eV along with satellite peaks at 785.5 eV and 802 eV, indicating the presence of Co^{2+} ions. For the O(1s) state, in **figure 3.4(d)**, there are two prominent peaks observed: one at 530.8 eV attributed to the metal-oxygen bond, Co-O, and the other at 532.14 eV, due to adsorbed water[42-43]. In the P(2p) peak in **figure 3.4(e)**, there is the deconvolution into two components, namely, the $2p_{3/2}$ and $2p_{1/2}$ at the respective binding energies of 133.09 eV and 134.05 eV, respectively, that validates the presence of P^{5+} ions within the unit $-PO_4$.[42]

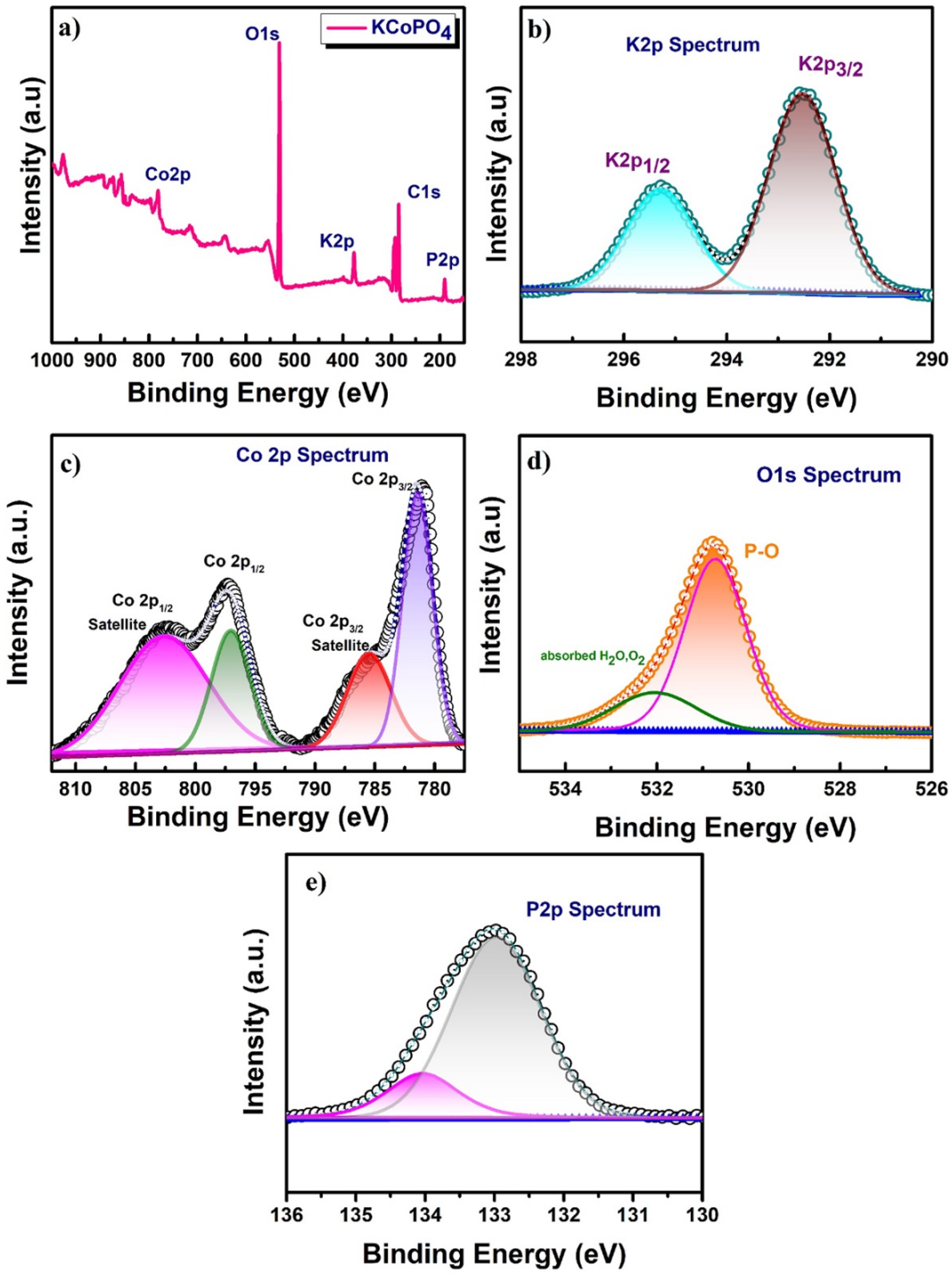

Figure 3.4: (a) XPS wide survey spectrum of $KCoPO_4$, and high-resolution spectra of (b) K (1s), (c) Co (2p), (d) O (1s), and (e) P (2p).

3.3.6 SEM/EDX Study

The FE-SEM image is shown in **figure 3.5(a)** displays particle size distribution and polyhedral morphology of $KCoPO_4$ powder and surface structure of the $KCoPO_4$ power sample suggesting an average particle size of 413 nm. **Figure 3.5(b)** represent the elemental analysis of the $KCoPO_4$ sample in the form of an Energy Dispersive X-ray Analysis (EDX) image which shows the peaks of all elements such as K, Co, P, and O present in $KCoPO_4$ sample. **Figure 3.5(c-f)** exhibits elemental mapping of $KCoPO_4$ compound and shows the results which indicate all the elements K, Co, P, and O, are present in the sample.

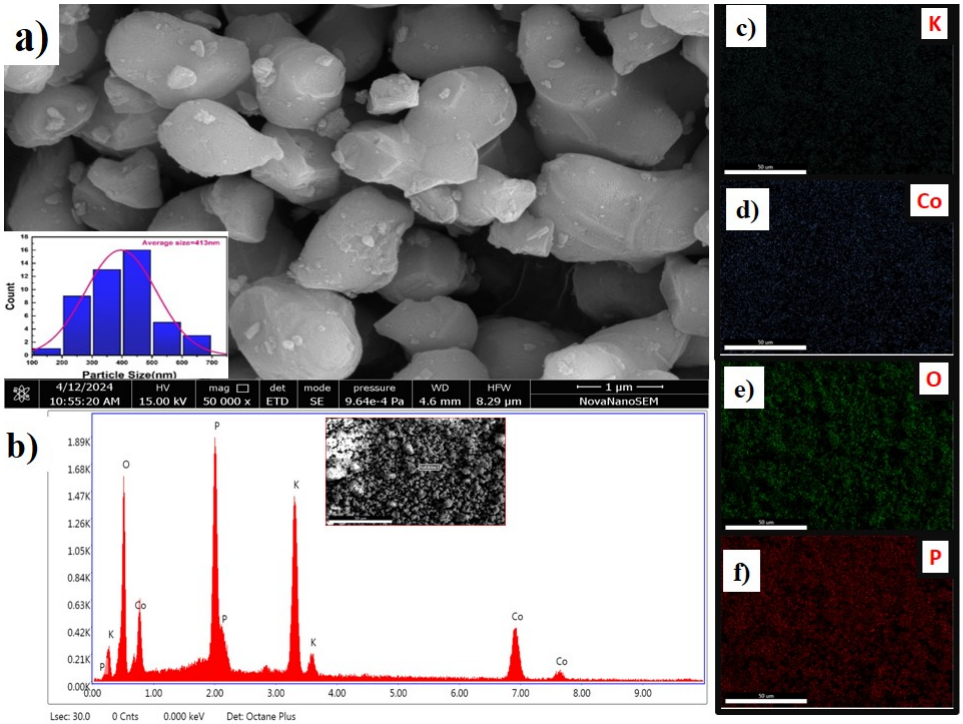

Figure 3.5: (a) FE-SEM images and (b) EDX analysis image of the prepared sample of $KCoPO_4$ sample (c-f) Element mapping of $KCoPO_4$

3.3.7 High-resolution transmission electron microscopy (HRTEM) study

High-resolution transmission electron microscopy (HRTEM) images of the $KCoPO_4$ sample are shown in **figure 3.6(a)** indicates the lattice fringes and **figure 3.6(a) (i - ii)** displaying the FFT (fast Furrier transformation) and inverse FFT image. **Figure 3.6(b)** shows the lattice

fringes of $KCoPO_4$ which is designated to the (220) plane of the $KCoPO_4$. The calculated d spacing value was found to be 0.455 nm for **figure 3.6(a)**. The crystalline nature of the sample is confirmed as the lattice fringes of this region revealed by the inverse fast Fourier transform (FFT) mapping using Gatan Digital Microscopy software.

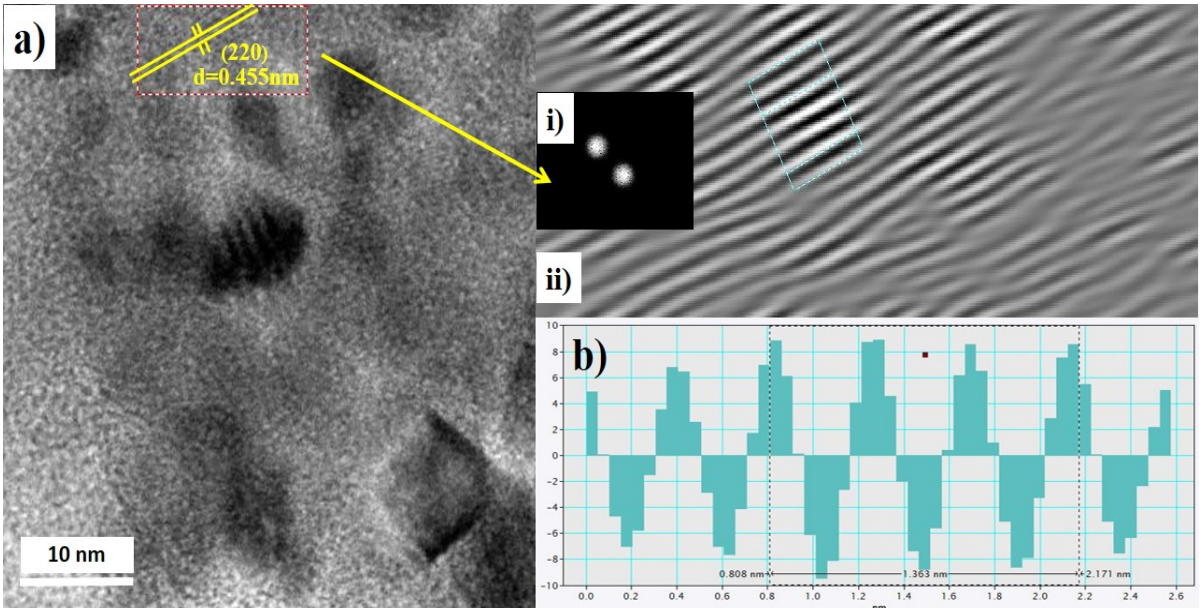

Figure 3.6: (a) Visible lattice fringes containing 220 planes in the HRTEM image, with (i and ii) FFT and inverse FFT images of the selected region of the (220) plane. (b) d spacing of fringes that matches with the (220) plane of the KCoPO4 lattice

3.4 Electrochemical Studies

3.4.1. Half-cell (three-electrode electrochemical cell) measurements

Electrochemical performance study of $KCoPO_4$ was characterized via a three-electrode system. In which, fluffy carbonized $KCoPO_4$ was utilized as the working electrode, platinum wire used as counter electrode, and saturated calomel Hg/HgO (1M KOH) was used as reference electrode, and 2M KOH taken as the electrolyte for this testing. The cyclic voltammetry (CV) analysis of $KCoPO_4$ display the essential electrochemical features, including redox activity and the shape of the curve within a potential range of 0 V to 0.5 V. **Figure 3.7(a)** shows the CV curve of $KCoPO_4$, which displays redox-mediated pseudo-capacitive charge storage behavior. [21-25]

The observed redox peaks are due to the reversible interconversion of Co^{2+} to Co^{3+} and the electrosorption of OH^- ions, as described by equation (3.1).

Redox-mediated diffusion-controlled intercalation

$$KCo(II)PO_4 + OH^-_{sol} \leftrightarrow KCo(III)(OH^-)PO_4 + e^- \quad (3.1)$$

EDLC-type surface capacitance:

$$KCo(II)PO_4 + xKOH \leftrightarrow K^+_x \,|\, KCo(II)PO_4 \,|\, xOH^- \quad (3.2)$$

Total charge storage capacity:

$$KCo(II)PO4 + xKOH + xOH^- \leftrightarrow K_x^+ \,|\, KCo(II)PO_4 \,|\, OH^-_{(1+x)} + xe^- \quad (3.3)$$

From the CV curve, the specific capacitance C (F/g) can also be calculated as one of the significant parameters to understand the electrochemical performance of the working electrode. The formula for the calculation of specific capacitance is given in equation (3.4).

$$Csp = \frac{\int i\,(V)dV}{mV\vartheta} \quad (3.4)$$

Where 'm' is the active mass on the working electrode (g), 'V' is the operating voltage window (V) of CV curve, and 'ϑ' is the scan rate (mV/s).

The specific capacitance of $KCoPO_4$ calculated by using equation (3.4) was found to be 788 F/g at 1 mV/s scan rate, and it dropped to 427 F/g at 100 mV/s. In the whole scan rate range, a pair of redox peaks was seen that exhibited a remarkable shift in the peak positions with the increasing scan rate. This shift in the anodic and cathodic peaks followed a linear relationship with the scan rate, thus indicating the predominant diffusion-controlled, intercalative redox-mediated charge storage mechanism in this material.[23]

As illustrated in **figure 3.7(b)**, anodic and cathodic peak currents vary directly with the square root of scan rate, proving the quasi-diffusion-controlled redox character of the $KCoPO_4$

electrode. The analysis of the electrode kinetics further gets authenticated by the Randles-Sevcik equation that provides useful information about the ion diffusion coefficient within the electrode. The diffusion coefficient of the ion inside the electrode was analyzed using the Randles-Sevick equation presented below.[21] – [23]

$$i_p = 2.686 \times 10^5 \times n^{3/2} A D^{1/2} C_o v^{1/2} \quad (3.5)$$

Where i_p is peak current density (A), n is the number of electrons that participated in the redox reaction (usually 1), A is the area of the electrode in cm^2, D is diffusion coefficient in cm^2/s, C_o is OH^- ion concentration in mol/cm^3 and ν is scan rate in V/s. By using equation (3.5), the diffusion coefficient (D) of OH^- in the $KCoPO_4$ electrode was found to be 2.56×10^{-9} cm^2/s for the oxidation reaction and the diffusion coefficient (D) value for the reduction reaction found to 1.83×10^{-9} cm^2/s.

To further understand the electrochemical kinetics of charge storage behaviour of electrodes in aqueous electrolytes, or to understand the qualitative nature of the charge storage mechanism of $KCoPO_4$ electrode by investigating the correlative contribution of the battery type or the capacitive type nature using the power-law equation given below in equation (3.6).

$$i = a\nu^b \quad (3.6)$$

Where, a and b are adjustable parameters, i is the current (A), and ν is the scan rate (V/s). The values of b range from 0.5 to 1 b = 0.5 stands for the intercalative semi-infinite diffusion control redox process or battery-type charge storage behaviour while b = 1 stands for the capacitive control reaction.

For the determination of b value **figure 3.7(c)** shows the log (peak current (i_p) vs log (v) plots and from the slope that plot, b values are extracted. From that instance, for scan rates of 1mv/s

to 100mv/s, the b-value of current observed for anodic peak is found close to 0.68 and for the cathodic peak it was found close to 0.74, that value indicating the rate kinetics are controlled by diffusion control surface redox is dominating.

Figure 3.7(d) shows the dependency of Voltammetry sweep rate on the current density plot that can quantitatively extract the capacitive contribution to the current density. The current density at a fixed potential for the calculation of the total capacitive contribution using the equation by Dunn equation (3.7).[21] – [23], [44]

$$i(\upsilon) = k_1 v + k_2 v^{\frac{1}{2}} \tag{3.7}$$

Equation (3.7) was simplified into equation (3.8) to analyze the independent charge contributions.

$$\frac{i(\upsilon)}{\upsilon^{\frac{1}{2}}} = \frac{k_1}{\upsilon^{\frac{1}{2}}} + k_2 \tag{3.8}$$

Where $k_1 v$ stands for capacitive control contribution and $k_2 v^{\frac{1}{2}}$ denotes diffusive control contribution. Thus, after the extraction of k_1 and k_2 from equation (3.8), individual contributions of diffusive and capacitive contribution at particular potentials can be measured. The values of k_1 and k_2 are measured from the slope and intercept of the $i(V)/v^{1/2}$ vs. $v^{1/2}$ plot represented in **figure 3.7(d)**. In **figure 3.7(e)** the capacitive-controlled contributions of 63% approximately and the diffusion-controlled of nearly 37% shown at the scan rate of 10 mV s^{-1}. The total contribution due to capacitive charge storage and total contribution due to diffusion controlled intercalative charge storage at various scan rates are shown in **figure 3.7(f)**, on the movement from low scan rate to high scan rate, the capacitance effect's contribution fraction significantly improves. This pseudocapacitive charge storage contribution comes from reversible intercalation/deintercalation of OH^- ion.

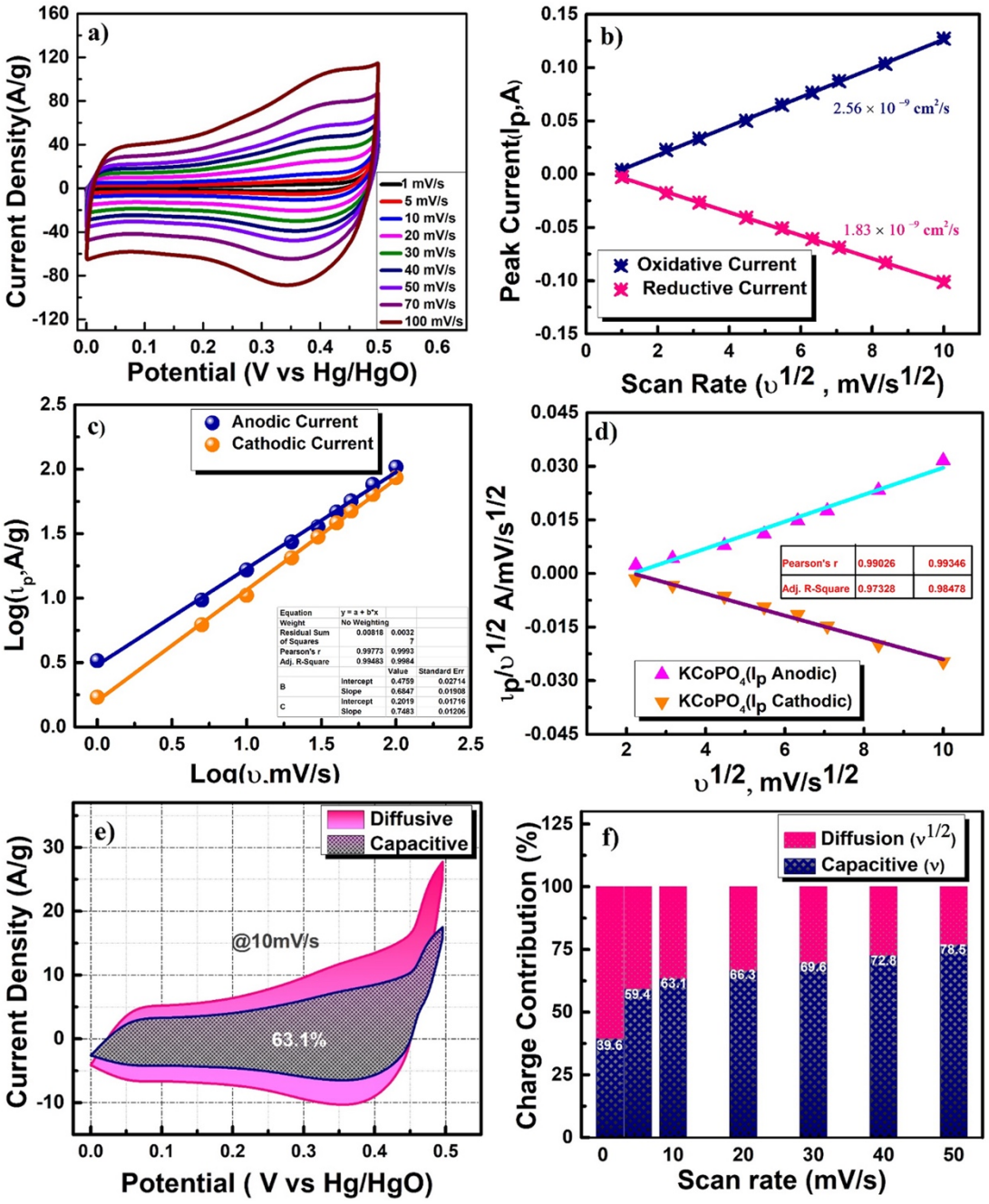

Figure 3.7: (a) CV curve for $KCoPO_4$ electrode in 2 M KOH solution at different scan rates (1–100 mV/s), **(b)** Peak current vs. square root of the scan rate plot of $KCoPO_4$ electrode. **(c)** power law plot of log(peak current) versus log(scan rate) indicating *b* values **(d)** Dunn method for capacitive and diffusion control process contribution in the current density at 10 mV/s of scan rate **(e)** Capacitance contribution at 10 mV/s **(f)** Diffusive and capacitive contribution of the electrode at various scan rates.

Additionally, the amount of charge stored in the outer and inner surfaces was calculated using the Trasatti plot. As suggested by Trassati, the total charge storage capacitance of a material is

the aggregate of the inner and outer surface contribution to the capacitance of the electrode and is represented by equation (3.9).

$$C_{total} = C_{in} + C_{out}\ (F/g) \qquad (3.9)$$

The Trasatti plot is used to evaluate the accessible inner (bulk) and outer surface charges which explains the specific capacitance of $KCoPO_4$ electrode materials. In **figure 3.8(a)**, the y-intercept of the linear fit of C^{-1} versus $v^{1/2}$ at different scan rates represents the total charge stored by the electrode or the total capacitance of the electrode. As seen in **figure 3.8(b)**, the y-intercept of the linear plot of C versus $v^{1/2}$ curve corresponds to the outer surface charge contribution to the charge storage or outer capacitance (C_{out}) of the electrode. Thereupon, by using the Trasatti plot, the total specific capacitance (C_{total}) of the electrode was found to be around 787 F/g at a scan rate of 1 mV/s. In conclusion, the inner surface contribution of total capacitance (C_{in}) was 368 F/g, accounting for 46.2% of the total capacitance while outer surface contribution (C_{out}) was 419 F/g, accounting for 53.8% at the same scan rate of 1 mV/s.

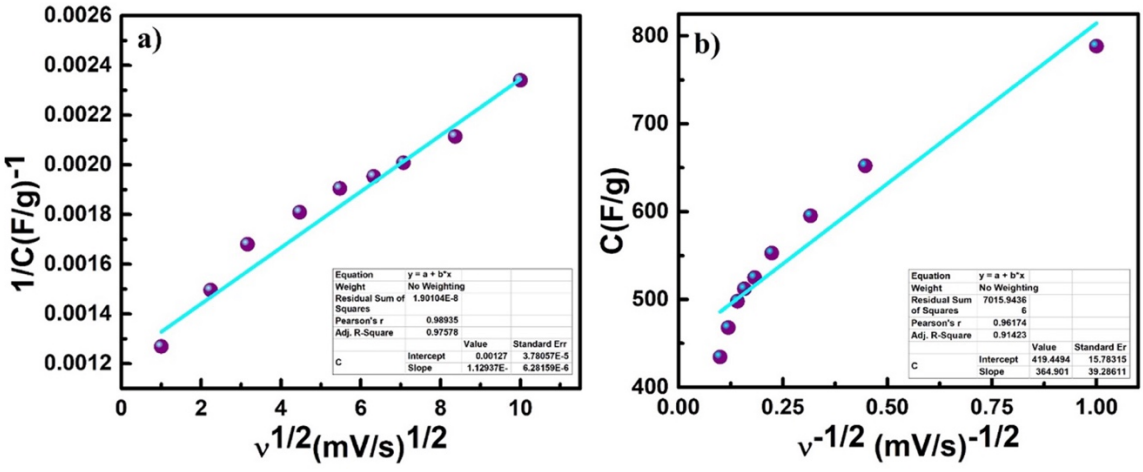

Figure 3.8: Trasatti plot (a) C^{-1}*vs.* $v^{1/2}$ and (b) *C vs.* $v^{-1/2}$ at a different scan rate

For a more accurate capacitance assessment of $KCoPO_4$ electrode sample galvanostatic experiments were performed. Galvanostatic charge/discharge studies were performed to get a quantitative value of the capacitance of the $KCoPO_4$ electrode, from the charge-discharge curve, the specific capacitance of the electrode can be calculated using equation (3.10).[20] – [23]

$$Csp = \frac{I\Delta t}{m\Delta V} \quad (3.10)$$

Where 'I' is the discharge current density (A), Δt is the discharge time (s), m is the active mass of the electrode (g) and ΔV is the discharge potential window (V).

Figure 3.9(a) shows the galvanostatic capacity/capacitance data of $KCoPO_4$ electrodes recorded as capacitance of 725 F/g, 672 F/g, 643 F/g, 588 F/g, 526 F/g, 491 F/g, and 438 F/g at different current rates of 0.5, 0.75, 1, 2, 3, 5, and 10 A/g, respectively. The increasing in current rates dependence of the decrease in specific capacitance, which could be due to inadequate time for OH ions to disseminate within the internal surface of the electrode material, and it is demonstrated in **figure 3.9(b)**. When the current density increases from 0.5 A/g to 10 A/g, the charge storage capacitance drops to only 39.5% of the initial value. **Figure 3.9(c)** presents $KCoPO_4$ with remarkable cycling performance and shows 89% capacity retention at a current of 10 A/g up to 5000 cycles. Again, this **figure 8(c)** contains the electrode's coulombic efficiency (η=td/tc) as it stands about 96.2% for all 5000 charge-discharge cycles, therefore it has the high reversibility and resilience of this electrode. Finally, measurements of the AC electrochemical impedance spectroscopy (EIS) performed on fresh electrodes as well as after 5000 cycles as seen in Nyquist Plot **figure 3.9(d)**. The Nyquist plot that was measured at 10 mV over a frequency from 1 MHz to 0.1 Hz shows a characteristic of a semicircle followed by an almost straight line, denoting pseudocapacitive storage of charge of the material.[46-47] The high frequency region gives the electric series resistance (Rs), but the semicircle at a low frequency relates to the transfer resistance (Rct) at an electrode/electrolyte interface.

The Warburg impedance (W), which is also known as diffusion resistance, is indicated by the line gradient in the low-frequency region. In the fresh electrode EIS performed and it exhibit, series resistance (Rs) was 2.05Ω and charge transfer resistance (Rct) was 0.515 Ω, after 5000 cycles, series resistance (Rs) and charge transfer resistance (Rct) values increased to 2.19 Ω

and 0.721Ω, respectively, with a very little change in impedance parameters including value reveals minimal variation before and after 5000 cyclic performances, indicating the material's stability.

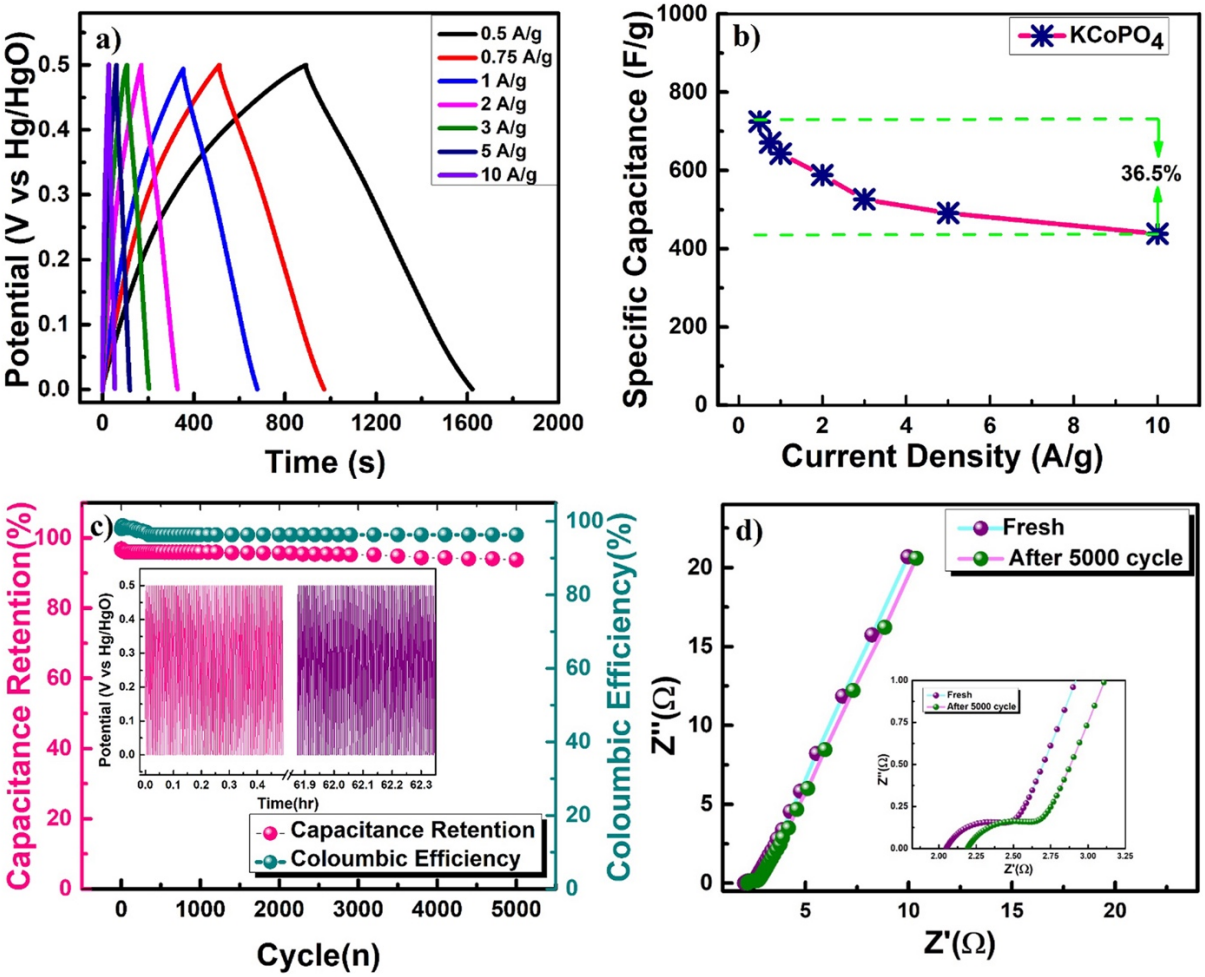

Figure 3.9: (a) Galvanostatic charge/discharge (V vs time) of the $KCoPO_4$ electrode at various current densities **(b)** Rate performance of the $KCoPO_4$ at different current densities, **(c)** Capacitance retention and Coulombic efficiency plot and **(d)** Nyquist plot at 10 mV applied voltage in the frequency range of 1 MHz to 0.1 Hz for before and after cyclibility.

3.4.2 Full cell measurements in Aqueous Asymmetric Supercapacitor (AASc) Mode

A full cell test was carried out using fluffy carbonized hexagonal $KCoPO_4$ as the positive electrode and Activated carbon as the negative electrode in two electrodes setup to explore the full potential of the fluffy carbonized hexagonal $KCoPO_4$, in a 2M KOH electrolyte in Aqueous Asymmetric Supercapacitor (AASc) mode. In order to obtain a high specific capacitance in the

full cell test, the capacitance storage of both electrodes must be balanced, as indicated by the following equation:

$$\frac{1}{C_{total}} = \frac{1}{C_{positive}} + \frac{1}{C_{negative}} \quad (3.11)$$

In order to maintain the charge storage capacitance of each electrode in balance within the cell, the mass ratio (m+/m-) of the two electrodes was determined using the following equation (3.12):

$$\frac{m^+}{m^-} = \frac{C_- \times \Delta E_-}{C_+ \times \Delta E_+} \quad (3.12)$$

Where as $m^+, m^-, C_+, C_-, \Delta E_+, \Delta E_-$ are active mass, specific capacitance, and potential window of both electrodes.

The individual CV curves of AC (activate carbon) (the negative electrode) and fluffy carbonized $KCoPO_4$ (the positive electrode). The mass ratio ($\frac{m^+}{m^-}$) of the electrodes was found to be 1:2.63 shown in the **figure 3.10(a)**. **Figure 3.10(b)** shows the CV curve of the AC//$KCoPO_4$ full cell in two electrodes (Asymmetric Supercapacitor configuration), tested at scan rates ranging from 5 mV/s to 100 mV/s within a potential window of 0V to 1.5V. **Figure 3.10(c)** displays the galvanostatic charge/discharge plot of the full cell, from which the actual specific capacitance of the cell was determined. The specific capacitance values were determined by using equation (3.10) and the values recorded as of 387 F/g, 360 F/g, 321 F/g, 163.5 F/g, 77.2 F/g, and 57.28 F/g at current densities of 1A/g, 2A/g, 3A/g, 5A/g, and 10A/g, respectively. **Figure 3.10(d)** displays coulombic efficiency for two-electrode cells, which dipped down to 91%, whereas the capacity retention was recorded at a capacity level of 86.3% after completing 5000 cycles at a specific applied load of 10A/g. **Figure 3.10(e)** reports EIS spectra, represented in the Nyquist plot. The data was measured before and after the cyclability test in frequencies within 1 MHz up to 0.1 Hz and at 10 mV/s applied potential. This suggests

that the series resistance of the plot increased from 2.25 Ω to 2.91 Ω while charge transfer resistance rose from 2.55 Ω to 3.1 Ω after 5000 cycles.

Charge storage capacity (energy density) and power capacity of full in AASc mode were calculated using the equations presented below:

$$E(Wh/kg) = \frac{1}{2}\frac{C_{ASCs}}{3.6}V^2 \quad (3.13)$$

$$P(W/kg) = \frac{E*3600}{t_{dis}} \quad (3.14)$$

Where C_{ASCs} is specific capacitance, V is Potential window and t_{dis} is discharge time.

Figure 3.10(f) shows energy density vs. power capacity as a function of constant current densities. The full cell attains the highest energy density of 121.1 Wh/kg at 1 A/g with the matching power capacity of around 667 W/kg. The maximum power density, 6945 W/kg, is realized at a lower energy density of 17.86 Wh/kg for the full cell under a current density of 10 A/g. These outstanding performance results for the $KCoPO_4$ electrode in a two-electrode AASc configuration mode confirm the promise of applicability for the development of high-performance EESDs in aqueous systems.[47] - [51]

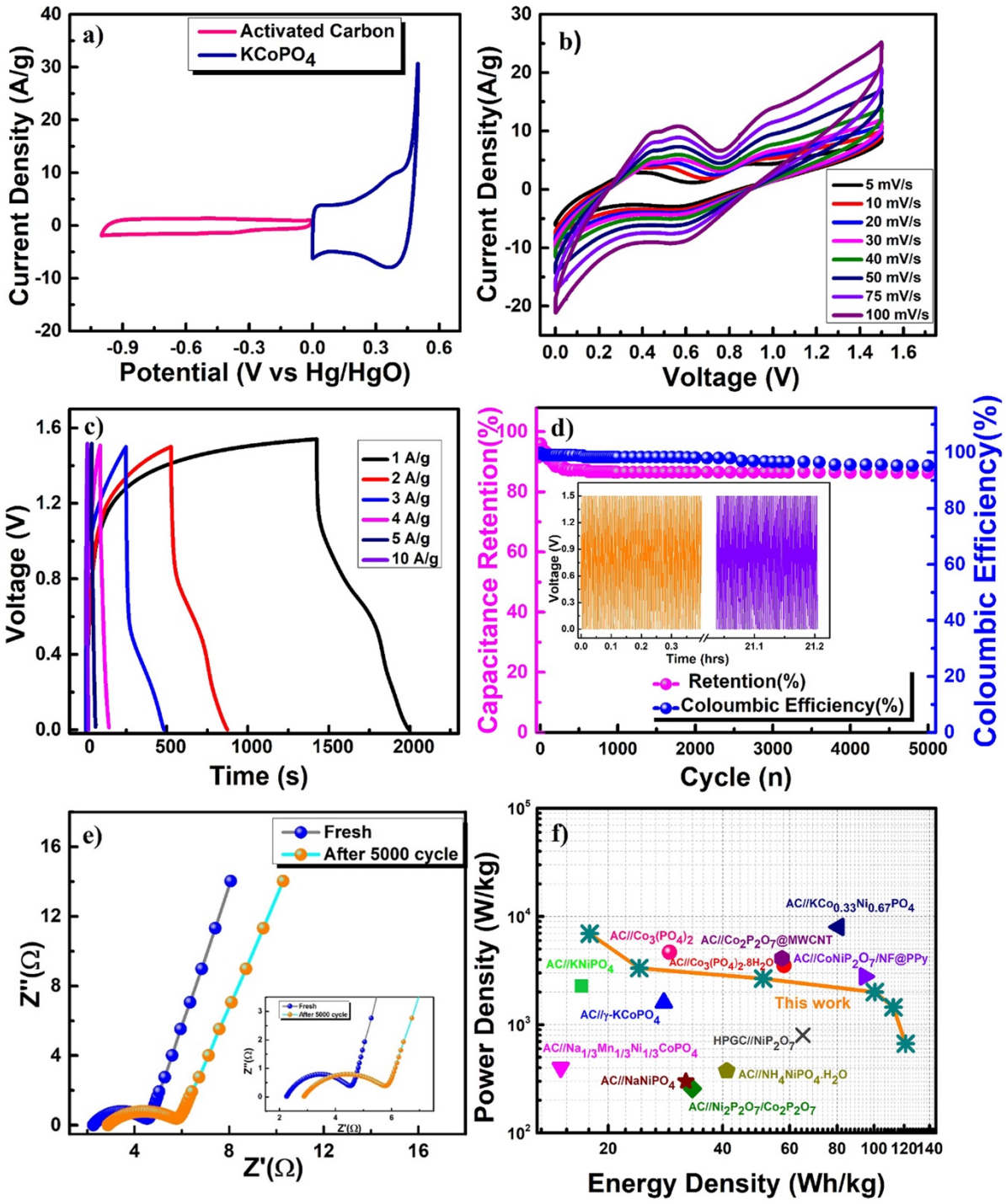

Figure 3.10: (a) CV curves AC and KCoPO4 electrode at 10 mV/s in a three-electrode system, (b) CV curves of AC//KCoPO4 as AASc in 2MKOH at different scan rates, (c) GCD curves of AC//KCoPO4 as AASc in 2MKOH at different current density, (d) capacitive retention and coulombic efficiency of the AASc device, (e) Nyquist at initial cycle and after 5000 cycles of the full cell in AASc mode (f) Ragone plot of AC//KCoPO4 as AASc with other literature reports.

3.5 Conclusions

The synthesis of fluffy carbonized hexagonal $KCoPO_4$ powder was successfully carried out with Maleic Acid as a chelating agent through a two-step process. It involved a sol-gel method and calcination at high temperatures to obtain a stable and crystalline structure. The prepared $KCoPO_4$ material was used as a positive electrode in half-cell configurations within an aqueous electrolyte to evaluate its electrochemical performance.

The excellent capacitance observed in $KCoPO_4$ electrodes has been mainly ascribed to a dominating intercalative pseudocapacitive mechanism for charge storage. This originates from the active role of Co^{2+}/Co^{3+} as an electroactive redox couple, which enables both intercalative (that is, bulk or interior) charge storage behavior and capacitive (surface-based) charge storage. In fact, intercalative mechanisms constituted 37% of total charge storage, whereas surface capacitive charge storage constitutes 63%.

The electrodes showed excellent long-term stability under aggressive cycling conditions. When cycled at a current density of 5 A/g for 5000 cycles, the $KCoPO_4$ electrodes retained 89% of their initial capacity retention, which shows excellent durability. The coulombic efficiency, an indicator of charge/discharge efficiency, was maintained at an impressive 92.7% even after prolonged cycling of 5000 cycles. This material fluffy carbonized $KCoPO_4$ was characterized to have a specific capacitance of 725 F/g with a current density of 0.5 A/g. It thus signifies a superior ability for charge storage as well as stability in low current density.

In addition, the wider context of this work is a comparison of the specific capacitance, energy density, and power density of our Aqueous Asymmetric Supercapacitor (AAS_C) devices with other reported transition metal phosphate-based AAS_C systems, as summarized in table 3.1.

To develop this $KCoPO_4$ material for its possible applications in the practical field, an Aqueous Asymmetric Supercapacitor (AASc) was fabricated. Here, the activated carbon (AC) served as the negative electrode while the positive electrode was prepared by the $KCoPO_4$ material. This

Asymmetric device, AC//$KCoPO_4$, offered remarkable electrochemical performance. Within a potential window of 1.5 V in 2M KOH aqueous electrolyte, the AASc resulted in a maximum energy density of 121.1 Wh/kg and also reached high power density value of 6945 W/kg. Most importantly, its full cell retained 86.3% of the capacity of its initial state by enduring 5000 cycles of charge-discharge operations, showing only 9% loss in coulombic efficiency.

The fabricated AASc device shows a number of notable advantages, including environmental friendliness, excellent rate performance, high energy density, and superior cycling stability-all at low cost. These attributes place the device in good stead for real-world energy storage applications.

Moreover, fluffy carbonized $KCoPO_4$ electrode has great potential for large-scale energy storage systems due to its excellent power performance, enhanced electrochemical energy storage capability, and superior long-term stability. Its suitability for grid-level applications underscores its ability to meet the demands of modern energy infrastructure, where reliable, sustainable, and high-performance energy storage solutions are essential.

Table 3.1: Electrochemical Capaciatnce of difeerent eelctrode in Full Cell

Electrode material (Negative Electrode//Positive Electrode)	**Electrolyte**	**Specific Capacitance**	**Energy Density/Power Density**	**Ref.**

AC//$KNiPO_4$	2M KOH	168.5 mAh/g (Capacitance: 935 F/g) at 1 A/g	ED=200 Wh/kg PD=819 W/kg	[23]
AC//γ-$KCoPO_4$	1M KOH	100 C/g at 0.6 mA/cm^2	ED=28 Wh/kg at PD=1600W/kg	[25]
AC// $NaMn_{1/3}Ni_{1/3}Co_{1/3}PO_4$	2M NaOH	45 F/g at 0.5A/g	ED=15 Wh/kg PD=400 W/kg	[29]
AC// $KCo_{0.33}Ni_{0.67}PO_4 \cdot H_2O$	1M KOH	227F/g at 1.5A/g	ED=80.64 Wh/kg at PW=8000 W/kg	[47]
AC// $Co_3(PO_4)_2 \cdot 8H_2O$	1M KOH	163 F/g at 2mA/cm^2	ED=58.12 Wh/kg at PW=3520 W/kg	[31]
AC// $Co_2P_2O_7$/MWCNT	1M KOH	114 mAh/g at 2.9A/g	ED=57.3 Wh/kg at PD=4100 W/kg	[32]
AC// $Co_3(PO_4)_2$	1M NaOH	111.2 F/g at 5mA/cm^2	ED=29.20 Wh/kg at PD= 4687 W/kg	[33]
HPGC//$Ni_2P_2O_7$	1M NaOH	183F/g at 1A/g	ED= 65 Wh/kg at PD=800W/kg	[41]
AC// $CoNiP_2O_7$/NF@PPy	2M KOH	390mAh/g at 2A/g	ED= 94.6Wh/kg at PD=2791W/kg	[48]
AC// $Ni_2P_2O_7/Co_2P_2O_7$	2M KOH	2074F/g at 5A/g	ED= 33.3 Wh/kg at PD= 257 W/kg	[49]
AC//$NH_4NiPO_4 \cdot H_2O$	3M KOH	1513 F/g at 5 A/g	ED= 41.6 Wh/ kg at PD= 375 W/kg	[50]
AC// $NaNiPO_4$	2M NaOH	90 F/g at 0.3A/g	ED= 32 Wh/kg at PD= 300 W/kg	[51]
AC//$KCoPO_4$	2M KOH	387F/g at 1A/g	ED=121 Wh/kg at PD= 6945 W/kg	This work

References

[1] E. Capacitors, “What Are Batteries, Fuel Cells, and Supercapacitors?,” 2004,104,4245-

4270, DOI: 10.1021/cr020730k.

[2] S. Chu and A. Majumdar, "Opportunities and challenges for a sustainable energy future," *Nature*,2012, 488, 294–303, DOI: 10.1038/nature11475.

[3] R. Eisenberg, "Addressing the Challenge of Carbon-Free Energy," *ACS Energy Lett.*, 2018, 3, 1521–1522, DOI: 10.1021/acsenergylett.8b00889.

[4] Z. Lv, W. Li, L. Yang, X. J. Loh, and X. Chen, "Custom-Made Electrochemical Energy Storage Devices," *ACS Energy Lett.*, 2019, 4, 606–614, 2019, DOI: 10.1021/acsenergylett.8b02408.

[5] X. Liu *et al.*, "Exploration in materials, electrolytes and performance towards metal ion (Li, Na, K, Zn and Mg)-based hybrid capacitors: A review," *Nano Energy*, 2021, 86, 106070, DOI: 10.1016/j.nanoen.2021.106070.

[6] L. Jiang *et al.*, "Building aqueous K-ion batteries for energy storage," *Nat. Energy*, 2019, 4, 495–503, DOI: 10.1038/s41560-019-0388-0.

[7] F. Wang, S. Xiao, Y. Hou, C. Hu, L. Liu, and Y. Wu, "Electrode materials for aqueous asymmetric supercapacitors," *RSC Adv.*, 2013, 3, 13059–13084, DOI: 10.1039/c3ra23466e.

[8] M. Chen, Y. Zhang, G. Xing, S. L. Chou, and Y. Tang, "Electrochemical energy storage devices working in extreme conditions," *Energy Environ. Sci.*, 2021, 14, 3323–3351, DOI: 10.1039/d1ee00271f.

[9] B. Pal, S. Yang, S. Ramesh, V. Thangadurai, and R. Jose, "Electrolyte selection for supercapacitive devices: A critical review," *Nanoscale Adv.*, 2019, 1, 3807–3835, DOI: 10.1039/c9na00374f.

[10] A. González, E. Goikolea, J. A. Barrena, and R. Mysyk, "Review on supercapacitors: Technologies and materials," *Renew. Sustain. Energy Rev.*, 2016, 1189–1206, DOI: 10.1016/j.rser.2015.12.249.

[11] Y. Jiang and J. Liu, “Definitions of Pseudocapacitive Materials: A Brief Review,” *Energy Environ. Mater.*, 2019, 2, 30–37, 2019, DOI: 10.1002/eem2.12028.

[12] P. Simon and Y. Gogotsi, “Materials for electrochemical capacitors,” *Mater. Sustain. Energy A Collect. Peer-Reviewed Res. Rev. Artic. from Nat. Publ. Gr.*, 2010, 138–147, DOI: 10.1142/9789814317665_0021.

[13] J. Ding, W. Hu, E. Paek, and D. Mitlin, “Review of Hybrid Ion Capacitors: From Aqueous to Lithium to Sodium,” *Chem. Rev.*, 2018, 118, 6457–6498, DOI: 10.1021/acs.chemrev.8b00116.

[14] N. R. Chodankar *et al.*, “True Meaning of Pseudocapacitors and Their Performance Metrics: Asymmetric versus Hybrid Supercapacitors,” *Small*, 2020, 16, DOI: 10.1002/smll.202002806.

[15] K. Subramanyan, M. L. Divya, and V. Aravindan, “Dual-carbon Na-ion capacitors: progress and future prospects,” *J. Mater. Chem. A*, 2021, 9, 9431–9450, DOI: 10.1039/d0ta12099e.

[16] R. Mondal, N. K. Mishra, M. Singh, A. Gupta, and P. Singh, “Perovskite La1−xKxCoO3−δ (0 ≤ x ≤ 0.5): a novel bifunctional OER/ORR electrocatalyst and supercapacitive charge storage electrode in a neutral Na2SO4 electrolyte,” *Phys. Chem. Chem. Phys.*, 2022, 24, 28584–28598, 2022, DOI: 10.1039/d2cp04708j.

[17] A. N. Singh, A. K. Yadav, A. Gupta, C. Rath, and P. Singh, “Fabrication and electrochemical performance of pseudocapacitive ABO2-type AgFeO2@C||K0.4MnO2. xH2O battery-type supercapacitive asymmetric cell for large-scale energy storage applications,” *J. Energy Storage*, 2023, 74, 109276, DOI: 10.1016/j.est.2023.109276.

[18] V. Kushwaha, R. Mondal, K. D. Mandal, P. Singh, and A. Gupta, “H2S Mediated One-Pot Synthesis of Single Phase Hexagonal CoS Nano-Spheres: A Pseudocapacitive

Electrode for Hybrid Supercapacitors," *ChemistrySelect*, 2023, 8, 2023, DOI: 10.1002/slct.202301349.

[19] V. Kushwaha, K. D. Mandal, A. Gupta, and P. Singh, "Ni0.5Co0.5S nano-chains: a high-performing intercalating pseudocapacitive electrode in asymmetric supercapacitor (ASC) mode for the development of large-scale energy storage devices," *Dalt. Trans.*, 2024, 5435–5452, DOI: 10.1039/d3dt04184k.

[20] N. K. Mishra, A. K. Singh, R. Mondal, and P. Singh, "NiC2O4 · 2H2O Nanoflakes: A Novel Redox-mediated Intercalative Pseudocapacitive Electrode for Supercapacitor Applications in Aqueous KOH and Neutral Na2SO4 electrolytes," *ChemistrySelect*, 2022, 7, DOI: 10.1002/slct.202201134.

[21] N. K. Mishra, R. Mondal, and P. Singh, "Synthesis, characterizations and electrochemical performances of anhydrous CoC2O4nanorods for pseudocapacitive energy storage applications," *RSC Adv.*, 2021, 11, 33926–33937, DOI: 10.1039/d1ra05180f.

[22] M. Singh, R. Mondal, P. Singh, and N. Sharma, "Framework structured Ce2(C2O4)3·10H2O as a pseudocapacitive electrode of a hybrid (asymmetric) supercapacitor (HSC) for large scale energy storage applications," *Phys. Chem. Chem. Phys.*, 2023,25, 11429–11441, DOI: 10.1039/d2cp05969j.

[23] M. Singh, S. Kumar, R. Mondal, P. Singh, R. Prakash, and N. Sharma, "Combustion-Synthesized KNiPO4: A Non-toxic, Robust, Intercalating Battery-Type Pseudocapacitive Electrode for Hybrid Supercapacitors as a Large-Scale Energy Storage Solution," *Energy and Fuels*, 2023, 37,4094–4105, DOI: 10.1021/acs.energyfuels.2c04092.

[24] N. Priyadharsini, A. Shanmugavani, L. Vasylechko, and R. Kalai Selvan, "Sol-gel synthesis, structural refinement, and electrochemical properties of potassium manganese

phosphate for supercapacitors," *Ionics (Kiel).*, 2018, 24, 2073–2082, DOI: 10.1007/s11581-018-2449-y.

[25] N. Priyadharsini, S. Surendran, B. Senthilkumar, L. Vasylechko, and R. K. Selvan, "Synthesis and Electrochemical Performances of γ-KCoPO4 Nanocrystals as Promising Electrode for Aqueous Supercapatteries," *ChemElectroChem*, 2019, 6, 369–377, DOI: 10.1002/celc.201801440.

[26] C. Masquelier and L. Croguennec, "Polyanionic (phosphates, silicates, sulfates) frameworks as electrode materials for rechargeable Li (or Na) batteries," *Chem. Rev.*, 2013,113, 6552–6591, DOI: 10.1021/cr3001862.

[27] L. M. Zhang *et al.*, "Hollow-Sphere-Structured Na4Fe3(PO4)2(P2O7)/C as a Cathode Material for Sodium-Ion Batteries," *ACS Appl. Mater. Interfaces*, 2021, 13, 25972–25980, DOI: 10.1021/acsami.1c04035.

[28] Y. Zhang, K. C. Kirshenbaum, A. C. Marschilok, E. S. Takeuchi, and K. J. Takeuchi, "Battery Relevant Electrochemistry of Ag7Fe3(P2O7)4: Contrasting Contributions from the Redox Chemistries of Ag+ and Fe3+," *Chem. Mater.*, 2016, 28, 7619–7628, DOI: 10.1021/acs.chemmater.6b02343.

[29] M. Minakshi,D. Meyrick, and D. Appadoo, "Maricite(NaMn1/3Ni1/3Co1/3PO4)/Activated Carbon: Hyrid Capacitor," *Energy Fuels* 2013, 27, 6, 3516–3522, DOI: 10.1021/ef400333s.

[30] N. Li, Q. Li, X. Guo, M. Yuan, and H. Pang, "Controllable synthesis of oxalate and oxalate-derived nanomaterials for applications in electrochemistry," *Chem. Eng. J.*, 2019, 372, 551–571, DOI: 10.1016/j.cej.2019.04.127.

[31] P. K. Katkar, S. J. Marje, S. S. Pujari, S. A. Khalate, A. C. Lokhande, and U. M. Patil, "Enhanced Energy Density of All-Solid-State Asymmetric Supercapacitors Based on Morphologically Tuned Hydrous Cobalt Phosphate Electrode as Cathode Material,"

ACS Sustain. Chem. Eng., 2019, 7, 11205–11218, DOI: 10.1021/acssuschemeng.9b00504.

[32] A. Agarwal, S. Majumder, and B. R. Sankapal, "Carbon Nanotube-Functionalized Surface-Assisted Growth of Cobalt Phosphate Nanodots: A Highly Stable and Bendable All-Solid-State Symmetric Supercapacitor," *Energy and Fuels*, 2022, 36, 5953–5964, DOI: 10.1021/acs.energyfuels.2c00600.

[33] H. Li, H. Yu, J. Zhai, L. Sun, H. Yang, and S. Xie, "Self-assembled 3D cobalt phosphate octahydrate architecture for supercapacitor electrodes," *Mater. Lett.*, 2015, 152, 25–28, DOI: 10.1016/j.matlet.2015.03.053.

[34] Y. Liu, Z. Li, Y. You, X. Zheng, and J. Wen, "Synthesis of different structured FePO4 for the enhanced conversion of methyl cellulose to 5-hydroxymethylfurfural," *RSC Adv.*, 2017, 7, 51281–51289, DOI: 10.1039/c7ra09186a.

[35] Gangulibabu, D. Bhuvaneswari, N. Kalaiselvi, N. Jayaprakash, and P. Periasamy, "CAM sol-gel synthesized LiMPO4 (M=Co, Ni) cathodes for rechargeable lithium batteries," *J. Sol-Gel Sci. Technol.*, 2009, 49, 137–144, DOI: 10.1007/s10971-008-1870-5.

[36] S. Vivekanandhan, M. Venkateswarlu, and N. Satyanarayana, "Ammonium carboxylates assisted combustion process for the synthesis of nanocrystalline LiCoO2 powders," *Mater. Chem. Phys.*,2008, 109, 241–248, DOI: 10.1016/j.matchemphys.2007.11.027.

[37] M. Thommes *et al.*, "Physisorption of gases, with special reference to the evaluation of surface area and pore size distribution (IUPAC Technical Report)," *Pure Appl. Chem.*, 2015, 87,1051–1069, DOI: 10.1515/pac-2014-1117.

[38] C. Schlumberger and M. Thommes, "Characterization of Hierarchically Ordered Porous Materials by Physisorption and Mercury Porosimetry—A Tutorial Review," *Adv. Mater.*

Interfaces, 2021, 8, DOI: 10.1002/admi.202002181.

[39] J. Wen *et al.*, "Constructing Multifunctional Metallic Ni Interface Layers in the g-C3N4 Nanosheets/Amorphous NiS Heterojunctions for Efficient Photocatalytic H2 Generation," *ACS Appl. Mater. Interfaces*, 2017, 9, 14031–14042, DOI: 10.1021/acsami.7b02701.

[40] T. Huang *et al.*, "Boosting Specific Energy and Power of Carbon Ionic Liquid Supercapacitor by Engineering Carbon Pores Structures," *Front. Chem,* 2020, 8, DOI: 10.3389/fchem.2020.00006.

[41] B. Senthilkumar, Z. Khan, S. Park, K. Kim, H. Ko, and Y. Kim, "Highly porous graphitic carbon and Ni2P2O7 for a high performance aqueous hybrid supercapacitor," *J. Mater. Chem. A*, 2015, 3, 21553–21561, DOI: 10.1039/c5ta04737d.

[42] B. Wu *et al.*, "Controlled solvothermal synthesis and electrochemical performance of LiCoPO4 submicron single crystals as a cathode material for lithium ion batteries," *J. Power Sources*, 2016, 304, 181–188, DOI: 10.1016/j.jpowsour.2015.11.023.

[43] G. Wang, Z. Yan, N. Wang, M. Xiang, and Z. Xu, "NiO/Ni Metal-Organic Framework Nanostructures for Asymmetric Supercapacitors," *ACS Appl. Nano Mater.*, 2021, 4, 9034–9043, DOI: 10.1021/acsanm.1c01628.

[44] R. Sahoo *et al.*, "Redox-Driven Route for Widening Voltage Window in Asymmetric Supercapacitor," *ACS Nano* 2018, *12*, 8494– 8505, DOI: 10.1021/acsnano.8b04040.

[45] S. Bhoyate *et al.*, "Eco-Friendly and High-Performance Supercapacitors for Elevated Temperature Applications Using Recycled Tea Leaves," *Glob. Challenges*, 2017, 1, 1–12, DOI: 10.1002/gch2.201700063.

[46] T. S. Mathis, N. Kurra, X. Wang, D. Pinto, P. Simon, and Y. Gogotsi, "Energy Storage Data Reporting in Perspective—Guidelines for Interpreting the Performance of Electrochemical Energy Storage Systems," *Adv. Energy Mater.*, 2019, 9, DOI:

10.1002/aenm.201902007.

[47] B. Liang *et al.*, "Controllable Fabrication and Tuned Electrochemical Performance of Potassium Co-Ni Phosphate Microplates as Electrodes in Supercapacitors," *ACS Appl. Mater. Interfaces*, 2018, 10, 3506–3514, DOI: 10.1021/acsami.7b14552.

[48] S. Sathishkumar *et al.*, "Bimetal Pyrophosphate of CoNiP2O7@polypyrrole Nanocomposite- Based Electrode for Hybrid Supercapacitor Applications," *Energy Technol.*, 2024, 2301589, 1–12, DOI: 10.1002/ente.202301589.

[49] P. Matheswaran, P. Karuppiah, S. M. Chen, and P. Thangavelu, "A binder-free Ni2P2O7/Co2P2O7nanograss array as an efficient cathode for supercapacitors," *New J. Chem.*, 2020, 44, 13131–13140, DOI: 10.1039/d0nj00890g.

[50] C. Chen *et al.*, "Polypyrrole-Modified NH4NiPO4·H2O Nanoplate Arrays on Ni Foam for Efficient Electrode in Electrochemical Capacitors," *ACS Sustain. Chem. Eng.*, 2016, 4, 5578–5584, DOI: 10.1021/acssuschemeng.6b01347.

[51] M. Minakshi Sundaram and D. R. G. Mitchell, "Dispersion of Ni2+ ions: Via acetate precursor in the preparation of NaNiPO4 nanoparticles: Effect of acetate vs. nitrate on the capacitive energy storage properties," *Dalt. Trans.*,2017, 46, 13704–13713, DOI: 10.1039/c7dt02444d.